Comput. Methods Appl. Mech. Engrg. 255 (2013) 89–103

Contents lists available at SciVerse ScienceDirect

Comput. Methods Appl. Mech. Engrg.

journal homepage: www.elsevier.com/locate/cma

A goal-oriented error estimator for the analysis of simplified designs

Ming Li [a,*], Shuming Gao [a], Kai Zhang [b]

[a] State Key Laboratory of CAD &CG, Zhejiang University, PR China
[b] Department of Mathematics, Jilin University, PR China

ARTICLE INFO

Article history:
Received 27 December 2011
Received in revised form 13 November 2012
Accepted 18 November 2012
Available online 29 November 2012

Keywords:
Defeaturing error
Analysis dependent simplification
CAD/CAE integration
Dual weighted residual

ABSTRACT

Simplifying an engineering design by removing geometric details can significantly reduce the complexity of downstream tasks of mesh generation and field solution computation. However, lack of a proper analysis and estimates of the errors induced by design simplification remains a bottleneck in seamless CAD/CAE integration. To address this issue, this paper develops a general framework for providing a posteriori estimates of goal-oriented engineering analysis error caused by removing a negative feature, or void, where material is absent, from an engineering design. Our approach is built upon the idea of representing it as a *modeling error* defined in the same geometry, which is then estimated using the dual weighted residual method. The derived error estimator still involves an uncomputable term involving dual errors, which is removed by further simplification into a term on the feature's boundary, via an exterior solution in linear cases or problem-specific approaches in nonlinear cases, utilizing classical theories of differential operators. We illustrate our approach via a semilinear second order elliptic equation, and explicit error estimators are also derived for the classical Poisson equation and linear elasticity. Results of numerical tests are shown, and comparisons made with results obtained with related approaches.

1. Introduction

Computer simulation, also referred to as engineering analysis, is typically performed using finite element analysis and related methods. It is based on a volumetric mesh derived by discretizing an engineering CAD model, the latter typically taking the form of a boundary representation (B-rep) model bounded by a set of NURBS surfaces. Converting such a CAD model into a volume mesh suitable for engineering analysis is far from trivial. It can take up to 80% of the overall analysis time for complex engineering designs according to a report from Sandia National Laboratories (see [5]).

One approach to resolving this formidable task of CAD/CAE integration is to use *isogeometric analysis* (IGA), proposed by Hughes et al. [24]. Here the same basis functions (usually NURBS, or alternatively, T-splines [5]) are used to represent the geometry *and* the solution space of dependent variables. The advantages of IGA for analysis are numerous: for example, exact geometry representation, simple mesh generation and refinement, and direct communication with CAD geometries [5,13,24,38,43]. Generating an IGA mesh for a single NURBS patch is straightforward, while doing so for a trimmed NURBS patch can generally be handled using T-splines [5,31,40] or trimming techniques [27]. Creating an IGA solid mesh for general 3D volumes is much more challenging, and recent progress toward this topic is referred to the work of Zhang et al. [48,50,51] or Xu et al. [49].

As well as mesh generation, CAD/CAE integration also involves a very time consuming and complex process called *geometry preparation* or *idealization*, which creates an analysis-suitable geometry via steps of dimension reduction [2,28,32] and geometry simplification. It typically requires much user interaction, and accounts for 57% of the overall analysis time at Sandia [5]; in comparison, mesh generation only accounts for 23% of the overall time. A major part of geometry simplification is *defeaturing*, removing geometric details such as holes, fillets, blends, and slots, from a complex CAD model. Doing so significantly reduces the time needed both for meshing and field solution computation performed on the mesh, and avoids potential mesh generation failure or ill-conditioned computations that may produce inaccurate analysis results. Consider for example, Fig. 1. The number of mesh elements used to represent the original geometry is much higher than for the simplified geometry (using the same meshing parameter settings), due to the requirements that the mesh should be adapted to the geometry, while having a smooth transition in element size.

The benefits of geometric simplification, however, come at the cost of (hopefully small) differences in the results of the analysis. Understanding the engineering analysis error induced by defeaturing, i.e., the *defeaturing error*, is essential if we are to ensure that a desired analysis accuracy can still be met after geometric simplification. Providing error estimates is necessary for both traditional finite element analysis and for the more novel IGA approach, as

* Corresponding author. Tel.: +86 571 88206681 525; fax: +86 571 88206680.
E-mail address: liming@cad.zju.edu.cn (M. Li).

0045-7825/$ - see front matter © 2012 Elsevier B.V. All rights reserved.
http://dx.doi.org/10.1016/j.cma.2012.11.010

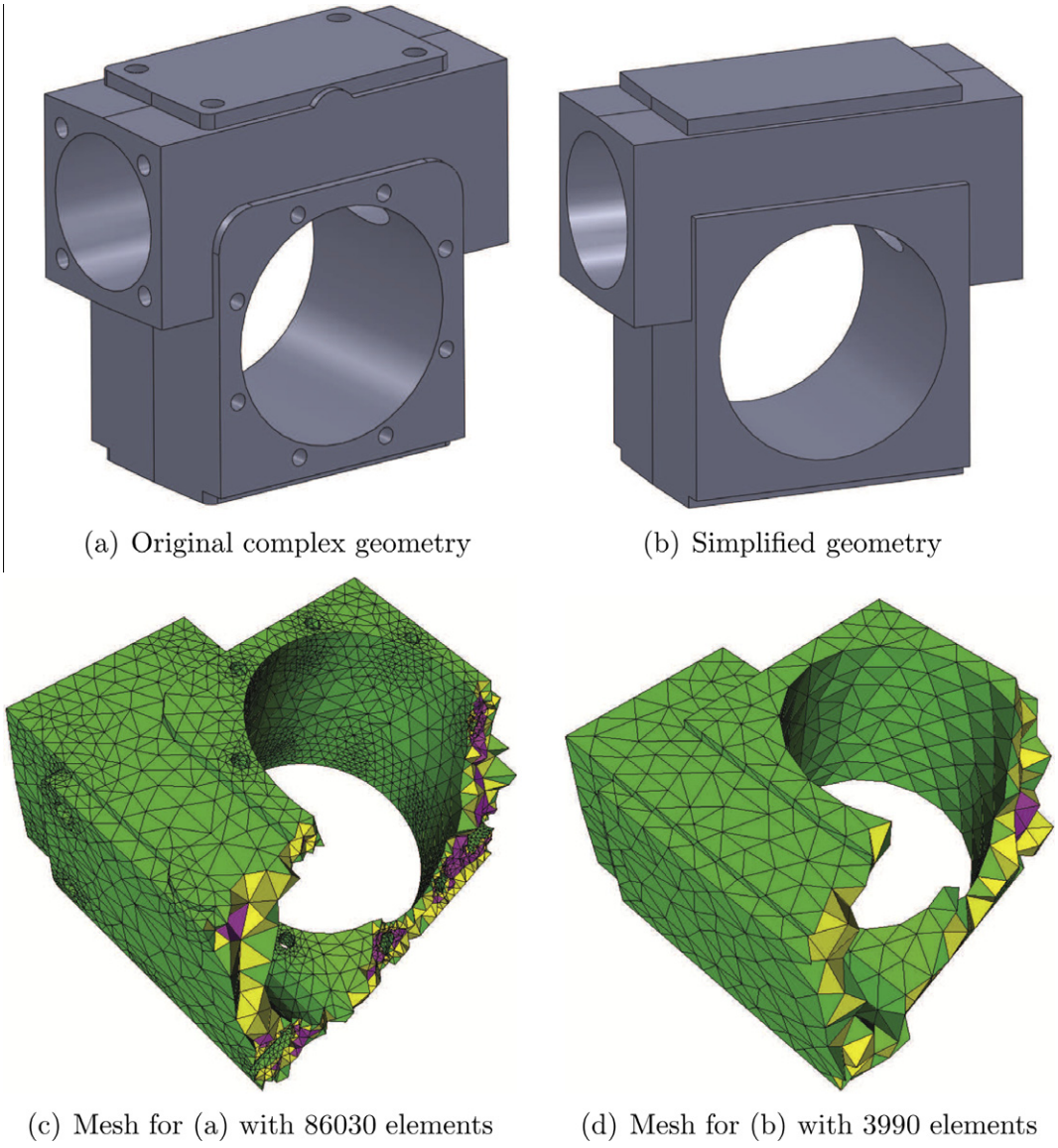

Fig. 1. Suppressing geometric details (36 holes, 8 blends and 2 extrusions) from the original complex geometry in (a) gives the simplified geometry in (b). Many fewer mesh elements are produced for the simplified geometry than the original geometry, given the same meshing parameters.

geometry simplification and idealization are still unavoidable for complex CAD models, as noted by Hughes et al. [24].

A full treatment of geometric simplification for engineering analysis is an extremely difficult task. This paper focuses on one of the core issues—providing proper estimates of changes in specific quantities of engineering interest due to the removal of a *negative feature*, or void, where material is absent, from an originally complex geometry. This *goal-oriented* error is estimated in an a posteriori sense by using analysis solutions for the simplified geometry but not solutions for the original complex geometry.

We give a general framework for a posteriori estimates of goal-oriented defeaturing errors for a broad class of linear and nonlinear physical phenomena. Our approach utilizes the *dual weighted residual* (DWR) method, originally developed by Becker and Rannacher [7] for finite element approximation error estimates, and extended by Oden and Prudhomme [35] to estimate modeling errors. By taking the solution for the simplified geometry as the solution restricted to the original geometry (as a sub-region of the simplified geometry), the defeaturing error is converted into a modeling error over the same geometry, caused by applying different boundary conditions over the internal boundary. This reformulated error can be then estimated using the DWR method, but this estimate still involves an uncomputable term of dual errors containing solutions for the original geometry. We thus further simplify the derived error estimate into a local quantity on the boundary of the negative feature. This simplification allows the dual error term to be estimated via an exterior solution in linear cases, or by utilizing classical theories of differential operators in nonlinear cases, ultimately resulting in an error estimate defined on the negative feature's boundary. We illustrate our overall approach using a semilinear second order elliptic equation, as well as deriving error estimates for the classical Poisson equation and linear elasticity. We also validate our results with numerical tests.

The idea of converting defeaturing error into modeling error was first described in [29] for linear elasticity, and extended in [30] for general nonlinear problems. However, both approaches are theoretically unjustified as they simply discard the uncomputable terms of the dual errors without attempting to estimate them. Unlike these approaches, here we estimate the dual error terms, using separate approaches for linear and nonlinear cases as noted above. As a result, our new error estimators (called *defeaturing error estimators* (DEEs)) are more widely applicable, and further

improve the accuracy of defeaturing error estimates, as shown in Section 5. We also show that they incorporate classical *topological sensitivity analysis* (TSA) as a special case for a Poisson equation. While [30] only considered the Poisson equation, here, error estimates are additionally provided for linear elasticity and the nontrivial case of semilinear second order elliptic equations.

1.1. Related work

Defeaturing error estimate is an important and difficult open problem [5,39,41,44]. Despite early recognition [25], this problem has been rarely directly addressed [20,22,45]. Other closely related work includes studies on TSA [42] and multiscale methods [14].

Traditional engineering analysis studies two major sources of errors: *approximation error* [26] and *modeling error* [35]. The former is due to the inherent inaccuracies involved in use of *discretized* mathematical models, while the latter is caused by imperfections in the mathematical models used to represent physical phenomena [35]. Studies of error estimates of both types generally assume that the underlying geometry in which analysis is performed remains unchanged (up to some tolerance) before and after approximation. The problem of estimating *defeaturing error*, where potentially large modifications are made to the underlying geometry, is rarely studied.

TSA estimates changes in solutions when an infinitesimal circular hole is created within an existing geometry [16,42]. Explicit analytical expressions have been derived for, e.g., the cases of Poisson equations [19], and linear elasticity with circular holes [34], or elliptic holes using the concept of a polarization tensor [3,33]. Recently, a practical, efficient numerical approach was devised for estimating TSA (called feature sensitivity analysis (FSA) there) induced by creating an arbitrarily-shaped small hole [22,46]. TSA has demonstrated its importance in design optimization, but it mainly focuses on infinitesimal geometry changes, and is hard to apply directly to the problem of finite-size geometry modification considered here. In order to handle this limitation, a second order TSA was recently derived in [18] for the Poisson equation, taking the total potential energy as cost function. Numerical comparisons of our estimates to those provided by classical TSA and FSA are shown in Section 5.

The concept of TSA is mainly concerned with a *single* negative feature, or void, where material is absent, the same as the problem studied in this paper. In contrast, multiscale methods [15,23,36] can simulate geometries containing *many* microscopic details, such as composite materials or porous media. The details are generally assumed to be periodic or statistically homogeneous distributions, or separable from the macroscopic problem, neither of which is assumed here. More closely related to the studied topic, Vemaganti [47] considered adaptive analysis of perforated materials in linear elasticity problems.

Heuristic approaches to defeaturing error estimates have been based on global energy differences [20]; this paper also studied protrusion details. However, an essential starting step there is that a local region has to be carefully selected around the suppressed feature to allow for local computation, and there is no obvious simple approach for doing this.

The remainder of the paper is organized as follows. The problem of estimating defeaturing error is stated in Section 2. Error estimates using DWR are described in Section 3, and goal-oriented error estimators are derived in Section 4. Numerical examples are presented in Section 5, and conclusions are drawn in Section 6.

2. Problem statement

Following previous work [30,45] on defeaturing error estimate, we assume that we consider (linear or nonlinear) engineering analysis problems defined over two different geometries, the *original geometry* and the *simplified geometry*. The original geometry typically has a complex structure and the field solutions defined over it are assumed to be very hard to compute or even intractable. The simplified geometry, with a much simpler structure, is obtained by removing geometric details from the original geometry, and the field solutions defined over it are much easier to determine (or may even be provided). This paper focuses on the simplification performed by removing negative features from a geometry. Clearly, in this case, the original geometry is contained within the volume of the simplified geometry.

Geometric differences between the original and simplified geometries cause differences in the solutions to the corresponding analysis problems, in turn affecting values of local quantities of interest. Our objective is to provide a general framework for computing an a posteriori estimate of goal-oriented defeaturing error caused by these differences in geometry.

Precisely, we have an original geometry $\Omega_\omega := \Omega \setminus \omega \in \mathbb{R}^n$ ($n = 2$ or 3) with ω being a prescribed negative feature to be removed. Removing ω from Ω_ω, we have the simplified geometry Ω: see Fig. 2. The analysis problem defined for the original geometry Ω_ω is: find the solution u_ω satisfying

$$\begin{cases} \mathcal{L}u_\omega = f & \text{in } \Omega_\omega, \\ \mathcal{B}u_\omega = d & \text{on } \partial\omega, \\ u_\omega = 0 & \text{on } \partial\Omega, \end{cases} \tag{1}$$

where $\partial\omega$ and $\partial\Omega$ denote the boundary of ω and Ω, respectively, $\mathcal{L}$ is some differential operator governing the physical phenomenon within the geometry interior, $\mathcal{B}v := \partial v/\partial n$, and f, d are functions with a compact support in Ω_ω or on $\partial\omega$, respectively. In Eq. (1), we take the boundary condition on $\partial\Omega$ to be homogenously Dirichlet for simplicity. All derivations in this paper work equally well for Neumann or homogeneous Dirichlet boundary conditions on $\partial\Omega$.

We specifically take

$$\mathcal{L}v := -\mathrm{div}(\nabla v) + \lambda v^3, \tag{2}$$

where $\lambda \geqslant 0$ is a non-negative parameter. In the above description, we restrict our attention to a specific semilinear second order elliptic boundary value problem [4] for ease of explanation and clarity. $\lambda \neq 0$ represents a nonlinear problem, while for $\lambda = 0, \mathcal{L}$ reduces to a classical linear Laplace operator. The basic framework approach used could also be extended to other nonlinear problems, but expressions for error estimates are problem-dependent and need to be derived for each specific case.

When suppressing the negative feature ω from Ω_ω, the associated boundary conditions on $\partial\omega$ are removed, and the boundary conditions on boundary $\partial\Omega$ remain unchanged. This ultimately results in a new analysis problem whose solution u satisfies

$$\begin{cases} \mathcal{L}u = f & \text{in } \Omega, \\ u = 0 & \text{on } \partial\Omega. \end{cases} \tag{3}$$

Now, let $Q(u)$ be a particular local quantity of interest prescribed over a region $S \subset \Omega_\omega$. We suppose $Q(u)$ can be written in a form

$$\mathcal{Q}(u) := \int_S q(u)dS, \tag{4}$$

where $q(\cdot)$ is some (linear or nonlinear) function with a compact support in S.

The goal-oriented defeaturing error caused by removing the negative feature is

$$e(\Omega_\omega, \Omega) := \mathcal{Q}(u_\omega) - \mathcal{Q}(u). \tag{5}$$

We wish to find an a posteriori estimate for this quantity by using the solution u defined over the simplified geometry Ω without directly using the solution u_ω defined over the original geometry Ω_ω.

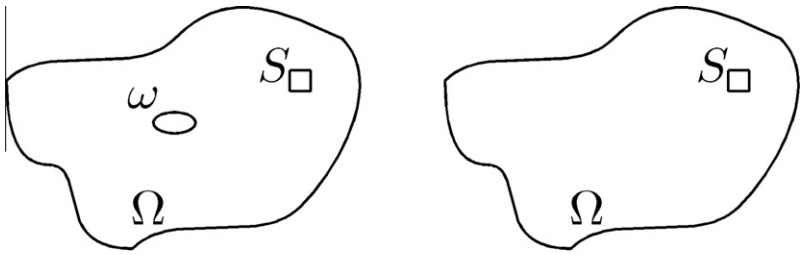

(a) Original geometry Ω_ω (b) Simplified geometry Ω

Fig. 2. An original geometry $\Omega_\omega = \Omega \setminus \omega$ containing a negative feature ω, and the simplified geometry Ω. S is a local region over which a quantity of interest is computed.

3. Goal-oriented defeaturing error estimate using DWR

In our approach, in Section 3.1, we show how the underlying geometric domains of solutions u_ω and u can be first unified into a single geometry Ω_ω, resulting in a new type of modeling error defined over this geometry. The error is then estimated using the DWR method in Section 3.2.

3.1. Error reformulation: from geometry difference to modeling difference

As the original geometry Ω_ω is contained within the simplified geometry Ω, i.e., $\Omega_\omega \subset \Omega$, the solution u in (3) is well defined in Ω_ω. Correspondingly, let

$$\bar{u}_\omega := u|_{\Omega_\omega}, \quad \bar{d} := \mathcal{B}u \quad \text{on } \partial\omega. \tag{6}$$

Thus, $\bar{u}_\omega$ satisfies the following equations:

$$\begin{cases} \mathcal{L}\bar{u}_\omega = f & \text{in } \Omega_\omega, \\ \mathcal{B}\bar{u}_\omega = \bar{d} & \text{on } \partial\omega, \\ \bar{u}_\omega = 0 & \text{on } \partial\Omega. \end{cases} \tag{7}$$

Comparing this with (1), the inner boundary term $\bar{d}$ in (7) is different from the term d in (1). Our error estimate is based on the observation that this difference is responsible for the defeaturing error.

The defeaturing error is derived using the associated weak forms of (1), (3) and (7). Before giving explicit expressions for these quantities, we introduce the following Sobelev spaces:

$$H^1(\Omega) := \{v \in L^2(\Omega) \Big| \frac{\partial v}{\partial x_i} \in L^2(\Omega), \quad i = 1, \ldots, n, \ n = 2 \text{ or } 3\},$$

$$H_0^1(\Omega) := \{v \in H^1(\Omega) | v = 0 \text{on} \partial\Omega\},$$

$$H_E^1(\Omega_\omega) := \{v \in H^1(\Omega_\omega) | v = 0 \text{on} \partial\Omega\}.$$

Then, the weak form of (3) is: find $u \in H_0^1(\Omega)$ such that

$$(\mathbf{P1}) \qquad \alpha(u, v) = l(v), \quad \forall v \in H_0^1(\Omega), \tag{8}$$

where

$$\alpha(u, v) := \int_\Omega (\nabla u \cdot \nabla v + \lambda u^3 v) dV, \quad l(v) := \int_\Omega f v dV.$$

The weak form of (1) is: find $u_\omega \in H_E^1(\Omega_\omega)$ such that

$$(\mathbf{P2}) \qquad \alpha_\omega(u_\omega, v) = l_\omega(v), \quad \forall v \in H_E^1(\Omega_\omega), \tag{9}$$

where

$$\alpha_\omega(u, v) := \int_{\Omega_\omega} (\nabla u \cdot \nabla v + \lambda u^3 v) dV - \int_{\partial\omega} d v \, d\Gamma,$$

$$l_\omega(v) := \int_{\Omega_\omega} f v dV.$$

And the weak form of (7) is: find $\bar{u}_\omega \in H_E^1(\Omega_\omega)$ such that

$$(\mathbf{P3}) \qquad \bar{\alpha}_\omega(\bar{u}_\omega, v) = l_\omega(v), \quad \forall v \in H_E^1(\Omega_\omega), \tag{10}$$

where

$$\bar{\alpha}_\omega(u_\omega, v) := \int_{\Omega_\omega} (\nabla u_\omega \cdot \nabla v + \lambda u_\omega^3 v) dV - \int_{\partial\omega} \bar{d} v \, d\Gamma.$$

The target quantity $Q(\cdot)$ is defined in $S \subset \Omega_\omega$, so equality of u and $\bar{u}_\omega$ in region Ω_ω lets us write that

$$\mathcal{Q}(u_\omega) - \mathcal{Q}(u) = \mathcal{Q}(u_\omega) - \mathcal{Q}(\bar{u}_\omega).$$

Thus, the defeaturing error on the left side, defined in two different geometries Ω_ω and Ω, has been converted into a modeling error on the right side, defined over just one geometry Ω_ω. By further noticing that the solutions $u_\omega, \bar{u}_\omega$ and their dual problem solutions (defined later) all lie in the same space $H_E^1(\Omega_\omega)$, the DWR method can be applied to find an error estimate.

We next introduce the *dual problems* related to the specific *primal problems* (**P1**)–(**P3**), for the local quantity of interest $\mathcal{Q}(\cdot)$. These dual problems are:

(1) Find the solution $p \in H_0^1(\Omega)$ satisfying

$$(\mathbf{D1}) \qquad \alpha'(u; v, p) = \mathcal{Q}'(u; v), \quad \forall v \in H_0^1(\Omega),$$

where $\alpha'(\cdot;\cdot,\cdot)$ and $\mathcal{Q}'(\cdot;\cdot)$ are Gâteaux derivatives [35], and $\alpha'(u; v, p)$ is given by

$$\alpha'(u; v, p) = \int_\Omega (\nabla p \cdot \nabla v + 3\lambda u^2 p v) dV.$$

(2) Find the solution $p_\omega \in H_E^1(\Omega_\omega)$ satisfying

$$(\mathbf{D2}) \qquad \alpha'_\omega(u_\omega; v, p_\omega) = \mathcal{Q}'(u_\omega; v), \quad \forall v \in H_E^1(\Omega_\omega), \tag{11}$$

where

$$\alpha'_\omega(u_\omega; v, p_\omega) = \int_{\Omega_\omega} (\nabla p_\omega \cdot \nabla v + 3\lambda u_\omega^2 p_\omega v) dV.$$

(3) Find the solution $\bar{p}_\omega \in H_E^1(\Omega_\omega)$ satisfying

$$(\mathbf{D3}) \qquad \alpha'_\omega(\bar{u}_\omega; v, \bar{p}_\omega) = \mathcal{Q}'(\bar{u}_\omega; v), \quad \forall v \in H_E^1(\Omega_\omega). \tag{12}$$

3.2. Defeaturing error estimate using DWR

First, we define residual functionals to characterize the degree to which $\bar{u}_\omega$ or $\bar{p}_\omega$ fails to satisfy the problem in (9) or (11) as

$$\mathcal{R}_P(\bar{u}_\omega; v) := l_\omega(v) - \alpha_\omega(\bar{u}_\omega; v), \quad v \in H_E^1(\Omega_\omega), \tag{13}$$

$$\mathcal{R}_D(\bar{u}_\omega, \bar{p}_\omega; v) := \mathcal{Q}'(\bar{u}_\omega; v) - \alpha'_\omega(\bar{u}_\omega; v, \bar{p}_\omega), \quad v \in H_E^1(\Omega_\omega), \tag{14}$$

The corresponding primal and dual errors $(e_P, e_D), (\bar{e}_P, \bar{e}_D)$ are

$$e_P := u_\omega - u, \quad e_D := p_\omega - p, \quad \bar{e}_P := u_\omega - \bar{u}_\omega, \quad \bar{e}_D := p_\omega - \bar{p}_\omega.$$

In particular,

$$\bar{e}_P = e_P, \quad \bar{e}_D = p_\omega - \bar{p}_\omega = 0, \quad \text{in } \Omega_\omega, \tag{15}$$

as only a Neumann boundary condition is prescribed on the internal boundary $\partial\omega$. This directly gives the following result for estimating the modeling error between u_ω and $\bar{u}_\omega$ (see [35]):

Proposition 1. *Let (u_ω, p_ω) be solutions to (9) and (11), and $(\bar{u}_\omega, \bar{p}_\omega)$ be solutions to (10) and (12). The a posteriori error can be written*

$$\mathcal{Q}(u_\omega) - \mathcal{Q}(\bar{u}_\omega) = \mathcal{R}_P(\bar{u}_\omega; p_\omega) + \frac{1}{2}\Delta\mathcal{R}_P + r(\bar{e}_P, \bar{e}_D),$$

where $\Delta\mathcal{R}_P$ and $r(\bar{e}_P, \bar{e}_D)$ are high-order terms with respect to $\bar{e}_P, \bar{e}_D$ defined below,

$$\begin{aligned}\Delta\mathcal{R}_P :=& \int_0^1 \alpha''_\omega(\bar{u}_\omega + s\bar{e}_P; \bar{e}_P, \bar{e}_P, \bar{p}_\omega + s\bar{e}_D)ds \\ &- \int_0^1 \mathcal{Q}''(\bar{u}_\omega + s\bar{e}_P; \bar{e}_P, \bar{e}_P)ds,\end{aligned}$$

and

$$\begin{aligned}r(\bar{e}_P, \bar{e}_D) :=& \frac{1}{2}\int_0^1 \{\mathcal{Q}'''(\bar{u}_\omega + s\bar{e}_P; \bar{e}_P, \bar{e}_P, \bar{e}_P) \\ &- 3\alpha''_\omega(\bar{u}_\omega + s\bar{e}_P; \bar{e}_P, \bar{e}_P, \bar{e}_D) \\ &- \alpha'''_\omega(\bar{u}_\omega + s\bar{e}_P; \bar{e}_P, \bar{e}_P, \bar{e}_P, \bar{p}_\omega + s\bar{e}_D)\}(s-1)s\, ds.\end{aligned}$$

The high-order terms $r(\bar{e}_P, \bar{e}_D)$ and $\Delta\mathcal{R}_P/2$ may be neglected if the errors $\bar{e}_P, \bar{e}_D$, or equivalently e_P (see (15)), are known to be small. Then replacing $\bar{u}_\omega$ with its equivalent value u in the above equation, we have

$$\mathcal{Q}(u_\omega) - \mathcal{Q}(u) \approx \mathcal{R}_P(u; p_\omega). \tag{16}$$

The error estimate in (16) involves the dual solution p_ω defined in Ω_ω, which was assumed to be uncomputable in our problem description in Section 2, as we must use solutions over the simplified geometry Ω but not over the original geometry Ω_ω. Deriving a computable error estimator from (16) is explained next.

4. Goal-oriented defeaturing error estimator

In this section, the estimate in (16) is first simplified to a local quantity defined on the boundary $\partial\omega$. By further dividing the adjoint solution p_ω into p and $e_D = p_\omega - p$ and noticing that p is computable, various defeaturing error estimators, can then be determined by estimating the uncomputable dual error e_D, using exterior approximation in linear cases, or other specific techniques in nonlinear cases.

Lemma 1. *The primal residual $\mathcal{R}_P(u; p_\omega)$ satisfies:*

$$\mathcal{R}_P(u; p_\omega) = \int_{\partial\omega} (d - \bar{d})p_\omega \, d\Gamma, \tag{17}$$

where $\bar{d}$ is defined in (6).

Proof. From the definition of $\mathcal{R}_P(\cdot;\cdot)$, we have

$$\mathcal{R}_P(u; p_\omega) = \alpha_\omega(u; p_\omega) - l_\omega(p_\omega) = \alpha_\omega(u; p_\omega) - \bar{\alpha}_\omega(\bar{u}_\omega; p_\omega).$$

Noting that $\bar{u}_\omega$ is the part of u defined in Ω_ω and using the expressions for $\alpha_\omega(\cdot;\cdot)$ and $\bar{\alpha}_\omega(\cdot;\cdot)$ in (9) and (10), we further have

$$\mathcal{R}_P(u; p_\omega) = \int_{\partial\omega} dp_\omega \, d\Gamma - \int_{\partial\omega} \bar{d}p_\omega \, d\Gamma = \int_{\partial\omega} (d - \bar{d})p_\omega \, d\Gamma,$$

as required. □

Combining (16) and (17) gives

$$\begin{aligned}\mathcal{Q}(u_\omega) - \mathcal{Q}(u) &\approx \int_{\partial\omega} (d - \bar{d})p_\omega \, d\Gamma \\ &= \int_{\partial\omega} (d - \bar{d})p \, d\Gamma + \int_{\partial\omega} (d - \bar{d})e_D \, d\Gamma.\end{aligned} \tag{18}$$

The first term $\int_{\partial\omega}(d - \bar{d})p \, d\Gamma$ is readily computable assuming that the functions u and p are explicitly known. Estimating the defeaturing error thus depends on estimating the value of the dual difference $e_D = p_\omega - p$—its exact computation is, in general, as complex as solving the original problem (1). However, it is only dependent on the value of e_D on the internal boundary $\partial\omega$, so specific approaches may be developed for estimating it.

In the following, we, respectively, explain approaches to estimating the dual error term in (18) for linear cases and nonlinear cases, or, respectively, $\lambda = 0$ or $\lambda > 0$ for $\mathcal{L}$ in (2).

4.1. Linear cases

We first consider the case when both the differential operator $\mathcal{L}$ and target quantity of interest $\mathcal{Q}$ are linear. In this case, $\lambda = 0$ in (2), and the dual operator of $\mathcal{L}$ is itself, i.e., $\mathcal{L}$ is self-adjoint.

It is then straightforward to derive the following governing equations for the dual error e_D,

$$\begin{cases} \mathcal{L}e_D = \bar{\mathcal{Q}}, & \text{in } \Omega_\omega, \\ \mathcal{B}e_D = g - \bar{g}, & \text{on } \partial\omega, \\ e_D = 0, & \text{on } \partial\Omega, \end{cases} \tag{19}$$

where $\bar{\mathcal{Q}} = 0$ in this particular case, g represents the boundary conditions for solution p_ω on the boundary $\partial\omega$, and $\bar{g} := \mathcal{B}p|_{\partial\omega}$.

Note that we are only interested in building an approximation to the value of e_D on the internal boundary $\partial\omega$ as required in (18). Assuming that the size of ω is much smaller than that of Ω, and it is far away from the outer boundary $\partial\Omega$, or $|\omega| \ll |\Omega|$ and $\text{dist}(\omega, \partial\Omega) \gg 1$, the value of $e_D|_{\partial\omega}$ can (by Lemma 2) be further approximated by an exterior solution e_E satisfying

$$\begin{cases} \mathcal{L}e_E = \bar{\mathcal{Q}}, & \text{in } \mathbb{R}^n \setminus \omega, \\ \mathcal{B}e_E = g - \bar{g}, & \text{on } \partial\omega, \\ \lim\limits_{|x|\to+\infty} e_E(x) = 0. \end{cases} \tag{20}$$

Comparing the above two equations, (19) is defined over the original geometry Ω_ω and is thus difficult to compute. However, (20), defined over $\mathbb{R}^n \setminus \omega$, can be computed much more easily using boundary element analysis [6] or finite element analysis with infinite elements [9].

To show the approximation between e_D and e_E, the following lemma first builds an upper bound of the difference between e_D and e_E using the so-called *perfectly matched layer method* [8] (*PML*). Suppose Ω_ω is centering at the origin O. Let $\rho_2 > \rho_1 > 0$ be two real numbers such that the balls $B_{\rho_1}(O), B_{\rho_2}(O)$ (centering at point 0 of radii ρ_1 and ρ_2) bound Ω. The PML is constructed in $B_{\rho_2}(O) \setminus \overline{B_{\rho_1}(O)}$, and let e_{pml} be the PML solution defined over $B_{\rho_2}(O) \setminus \omega$, and real numbers $\sigma_0 > 0$, integer $m \geqslant 1$ be constant parameters of the PML (we always adopt $\sigma_0 \approx 10^3$ and $m = 3, 4$ or 5 for practical purposes). We have the following result.

Lemma 2. *Let e_D and e_E be the solutions of (19) and (20), we have*

$$\begin{aligned}\|e_D - e_E\|_{L^2(\partial\omega)} \leqslant\ & C_1 \exp\left(-\frac{C_2\sigma_0\delta}{m+1}\left(1 - \frac{(m+1)\rho_1^2}{\sqrt{(m+1)^2\rho_2^2 + \sigma_0^2\delta^2}}\right)^{1/2}\right) \\ &+ \|\overline{G}\|_{L^2(\Omega_\omega)}\|\bar{\mathcal{Q}}\|_{L^2(\Omega_\omega)} + \|\overline{G}\|_{L^2(\partial\omega)}\|\mathcal{B}p\|_{L^2(\partial\omega)},\end{aligned} \tag{21}$$

where C_1, C_2 are positive constants, $\delta := \rho_2 - \rho_1, \overline{G}(\cdot,\cdot) := G_D(x - \cdot, y - \cdot) - G_{pml}(x - \cdot, y - \cdot)$ for the two fundamental solutions

G_D to (19) and G_{pml} to the corresponding PML problem for (20); further details are referred to Appendix A.

From the result in Lemma 2 and the property of PML, the first term of the right hand side of (21) can be small if we choose δ small and $\delta\sigma_0$ large enough. Additionally, under the assumptions $|\omega| \ll |\Omega|$ and $\mathrm{dist}(\omega, \partial\Omega) \gg 1$, we can also set δ small enough to guarantee the difference between G_D and G_{pml} is tiny, which leads to the second and third terms of (21) being small. Correspondingly, the difference between e_E and e_D can always be small. The numerical results in Section 5 further complement this result. It is also observed in Section 5 that even when these assumptions are not valid, the estimated defeaturing errors are often acceptable.

Based on the above analysis, replacing e_D by its approximation e_E in (18), gives the following defeaturing error estimate for linear cases:

Proposition 2. *Under the assumption of Lemma 2, for a linear operator $\mathcal{L}$(or $\lambda = 0$ in (2)) and a linear target quantity $\mathcal{Q}(u)$, we have*

$$(\textbf{DEE} : \textbf{Poisson}) \quad \mathcal{Q}(u_\omega) - \mathcal{Q}(u) \approx \int_{\partial\omega} (d - \bar{d})(p + e_E)\, d\Gamma, \tag{22}$$

where e_E is computable by (20).

Remark 1. The proposed estimator in (22) actually includes TSA as a special case. For simplicity, we illustrate this idea with ω being a circular hole of radius r centered at point $\boldsymbol{P}_C$, for which TSA [3,19] gives

$$\mathcal{Q}(u_\omega) - \mathcal{Q}(u) = \pi r^2 (2\nabla u_\omega \cdot \nabla p_\omega - f p_\omega)|_{\boldsymbol{P}_C}. \tag{23}$$

Under the assumption that $|\omega| \ll |\Omega|$ and $\mathrm{dist}(\omega, \partial\Omega) \gg 1$, we have

$$\begin{aligned}\int_{\partial\omega} (d - \bar{d}) p\, d\Gamma &= -\int_{\partial\omega} (\nabla u \cdot n) p\, d\Gamma = \int_\omega \nabla u \cdot \nabla p dV - \int_\omega f p dV \\ &= \pi r^2 (\nabla u_\omega \cdot \nabla p_\omega - f p_\omega)|_{\boldsymbol{P}_C} + O(r^2).\end{aligned}$$

Additionally, substituting the exterior solution for a point $\boldsymbol{P}$ along $\partial\omega$ and the center $\boldsymbol{P}_C$ of ω

$$e_E = \frac{r^2}{\|\boldsymbol{P} - \boldsymbol{P}_C\|^2} \nabla p \cdot (\boldsymbol{P} - \boldsymbol{P}_C),$$

giving

$$\int_{\partial\omega} (d - \bar{d}) e_E\, d\Gamma = -\int_{\partial\omega} (\nabla u \cdot n) e_E d\Gamma = \pi r^2 \nabla u_\omega \cdot \nabla p_\omega|_{\boldsymbol{P}_C} + O(r^2).$$

Combining the above two approximations gives the TSA result in (23).

Remark 2. The result in Proposition 2 can be extended without difficulty to the case of linear elasticity for a negative feature ω under external loading $\boldsymbol{d}$. Specifically, we have

$$\begin{aligned}&(\textbf{DEE} : \textbf{Elasticity}) \quad \mathcal{Q}(\boldsymbol{u}_\omega) - \mathcal{Q}(\boldsymbol{u}) \\ &\quad \approx \int_{\partial\omega} (\mathbf{d} - \bar{\mathbf{d}}) \cdot (\boldsymbol{p} + \boldsymbol{p}_E)\, d\Gamma,\end{aligned} \tag{24}$$

where $\bar{\mathbf{d}} = \partial\sigma(\boldsymbol{u})/\partial\mathbf{n}$, "$\cdot$" denotes inner product and $\boldsymbol{p}, \boldsymbol{p}_E$ are defined similarly to p, p_E above.

4.2. Nonlinear cases

Estimating the dual error for nonlinear cases, when $\lambda > 0$ for $\mathcal{L}$ in (2) or $\mathcal{Q}(u)$ is nonlinear, is more difficult than for linear cases. In the following, a linear approximation for the governing equation of e_D is first introduced, following the analysis in [35], for this purpose.

Lemma 3. *For $\mathcal{L}$ defined in (2), the dual error e_D satisfies:*

$$\alpha'_\omega(u; v, e_D) = \mathcal{R}_D(u, p; v) + \Delta\mathcal{R}_D, \quad v \in H^1_E(\Omega_\omega), \tag{25}$$

where $\mathcal{R}_D$ is the dual residual defined in (14), and

$$\Delta\mathcal{R}_D = \int_0^1 \alpha''_\omega(u + s e_P; e_P, v, p) ds - \int_0^1 \mathcal{Q}''(u + s e_P; e_P, v)\, ds.$$

Proof. Using the dual residual defined in (14), we can show that

$$\begin{aligned}\mathcal{R}_D(u, p; v) &= \mathcal{Q}'(u; v) - \alpha'_\omega(u; v, p) \\ &= \mathcal{Q}'(u; v) - \mathcal{Q}'(u_\omega; v) + \mathcal{Q}'(u_\omega; v) - \alpha'_\omega(u; v, p) \\ &= \mathcal{Q}'(u; v) - \mathcal{Q}'(u_\omega; v) + \alpha'_\omega(u_\omega; v, p_\omega) - \alpha'_\omega(u; v, p) \\ &= \mathcal{Q}'(u; v) - \mathcal{Q}'(u_\omega; v) + \alpha'_\omega(u_\omega; v, p_\omega) - \alpha'_\omega(u; v, p_\omega) \\ &\quad + \alpha'_\omega(u; v, p_\omega) - \alpha'_\omega(u; v, p) \\ &= -E_1 + E_2 + \alpha'_\omega(u; v, e_D)\end{aligned}$$

where

$$E_1 := \mathcal{Q}'(u_\omega; v) - \mathcal{Q}'(u; v) = \int_0^1 \mathcal{Q}''(u + s e_P; e_P, v)\, ds,$$

$$E_2 := \alpha'_\omega(u_\omega; v, p) - \alpha'_\omega(u; v, p) = \int_0^1 \alpha''_\omega(u + s e_P; e_P, v, p) ds.$$

Taking $\Delta\mathcal{R}_D := -E_1 + E_2$, the above lemma is verified. □

Using the linearization result in Lemma 3 generally simplifies the problem of estimating the dual error e_D for nonlinear problems. We summarize the error estimate result below; a proof of this result is given in Appendix B.

Proposition 3. *When $\lambda > 1$ in (2), the defeaturing error estimate is*

$$\begin{aligned}&(\textbf{DEE} : \textbf{Semilinear}) \quad \mathcal{Q}(u_\omega) - \mathcal{Q}(u) \\ &\quad \approx \int_{\partial\omega} (d - \bar{d}) p\, d\Gamma + C_N^2 \|g - \bar{g}\|_{L^2(\partial\omega)} \|d - \bar{d}\|_{L^2(\partial\omega)},\end{aligned} \tag{26}$$

where $d = \mathcal{B}u_\omega|_{\partial\omega}, g = \mathcal{B}p_\omega|_{\partial\omega}$ are, respectively, the prescribed boundary terms for the primal and dual solutions $u_\omega, p_\omega, \bar{d} := \mathcal{B}u|_{\partial\omega}, \bar{g} := \mathcal{B}p|_{\partial\omega}$, and C_N is a constant only dependent on the geometry of Ω_ω.

Remark 3. The exterior approximation for linear cases given in Section 4.1 can be extended to nonlinear cases due to the result in Lemma 3. Specifically, let $\mathcal{L}_1$ and $\mathcal{Q}_1$ denote the differential operators corresponding to α'_ω and $\mathcal{R}_D$, respectively. In the proof of Lemma 2, we assume that $\bar{\mathcal{Q}}$ in (19) has a compact support, i.e., supp $\bar{\mathcal{Q}} \subset \Omega_\omega$. This assumption now needs to be satisfied for $\mathcal{Q}_1$, which essentially corresponds to $\mathcal{R}_D(u, p)$ in (25). In order to resolve this, we can use a mollification kernel function $\delta(r)$ to mollify $\mathcal{R}_D(u, p)$ such that $\tilde{\mathcal{R}}_D(u, p) = \delta(r) * \mathcal{R}_D(u, p)$ has a compact support, where $*$ denote convolution. All results are valid for $\tilde{\mathcal{R}}_D(u, p)$ by similar arguments.

Remark 4. Discarding the term containing dual error e_D in (18) gives the error estimate in [30], that is,

$$(\textbf{Direct} : \textbf{Semilinear})\ \mathcal{Q}(u_\omega) - \mathcal{Q}(u) \approx \int_{\partial\omega} (d - \bar{d}) p\, d\Gamma \tag{27}$$

for the problem in (1), whether λ is equal to zero or not, or

$$(\textbf{Direct} : \textbf{Elasticity})\ \mathcal{Q}(\boldsymbol{u}_\omega) - \mathcal{Q}(\boldsymbol{u}) \approx \int_{\partial\omega} (\mathbf{d} - \bar{\mathbf{d}}) \cdot \boldsymbol{p}\, d\Gamma \tag{28}$$

in the case of linear elasticity.

A theoretical verification that (27) provides a good approximation of modeling errors can be found in [10]. The merit of using this simple estimator lies in the fact that it does not need the additional

computation effort to find e_E for different negative features, and is thus more efficient. Its performance will be compared with that of our newly derived estimator in Section 5.

5. Numerical examples

The proposed defeaturing error estimator (DEE) has been implemented on a 2.8 GHz dual quad-core processor with 4 GB RAM using COMSOL [1], a commercial finite-element based CAD/CAE system. Three different linear and nonlinear problems were considered: the Poisson equation, a linear elasticity problem, and the second order semilinear elliptic problem in (1) with $\lambda = 1$.

DEE was tested at variations of the negative feature's geometry, and in particular its size, center location, and shape, as well as for variations in imposed loadings. The obtained results were compared with the reference values (pseudo-ground truth) computed by direct finite element analysis (FEA) of the full model (ignoring discrete FE approximation errors). We used an FE space built from quadratic polynomials over an FE mesh generated using COMSOL's default settings, and the number of mesh elements and the degree of freedoms used to obtain these results are reported later after each specific example.

Numerical results were also compared with ones obtained by topological sensitivity analysis (TSA) [3,19,34], feature sensitivity analysis (FSA) [22,45], and results computed using (27) or (28), denoted Direct [30]; both the estimated errors e and the estimated quantities $\mathcal{Q}(u) + e$ were compared in all the examples. When computing the exterior solution p_E in (20), we simply replaced $\mathbb{R}^n$ with a sufficiently large square (specifically 10 times the size of the negative feature) around the negative feature ω. The exterior solution $\boldsymbol{p}_E$ was computed similarly.

The quality of an error estimator is usually measured in terms of its *effectivity index*, defined as the ratio between the estimated error e and the exact error $E = \mathcal{Q}(u_\omega) - \mathcal{Q}(u)$ with respect to a local quantity of interest $\mathcal{Q}(\cdot)$, that is

$$I := e/E. \tag{29}$$

When using a global energy norm, effectivity indices between 0.5 and 2.0 are often characterized as successful in the error estimate literature. However, accurate goal-oriented error estimates are generally very difficult or expensive to obtain [37], and in practice, effectivity indices up to 10 are still considered useful [21].

Average times taken to compute different estimates for the various numerical examples are summarized in Table 1.

5.1. Poisson equation

The classical Poisson equation ($\lambda = 0$ in (2)) is first considered. We compare our results given by DEE in (22) with those obtained by TSA [3,19], FSA [22] and Direct [30] (in the form of (27)). The error estimates provided by TSA and FSA are first explained for reference.

TSA [3]: for an elliptic hole with center $\boldsymbol{P}_C$ within the geometry, and semi-axes a and b parallel to the main axes of the coordinate system, TSA gives

$$(\textbf{TSA} : \textbf{Poisson}) \quad \mathcal{Q}(u_\omega) - \mathcal{Q}(u) = ab\pi(\nabla u^T \cdot T_\omega \cdot \nabla p - fp)|_{\boldsymbol{P}_C}, \tag{30}$$

where T_ω is defined as

$$T_\omega := \begin{pmatrix} 1 + a/b & 0 \\ 0 & 1 + b/a \end{pmatrix}.$$

FSA [22]: for an arbitrarily-shaped small hole centered at $\boldsymbol{P}_C$ and free from external loading, FSA gives

$$(\textbf{FSA} : \textbf{Poisson}) \quad \mathcal{Q}(u_\omega) - \mathcal{Q}(u) = \int_{\partial\omega} (\boldsymbol{V} \cdot \mathbf{n})(F_1 + F_2)\, ds \tag{31}$$

where

$$F_1 := \frac{fp - (\nabla u + \nabla u_E) \cdot (\nabla p + \nabla p_E)}{2}, \quad F_2 := \frac{fp_E}{3}, \quad \boldsymbol{V} := \boldsymbol{P} - \boldsymbol{P}_C$$

for a point $\boldsymbol{P}$ along the negative feature's boundary $\partial\omega$, where u_E, p_E are the corresponding primal and dual exterior solutions.

The test uses the example in Fig. 3 of an internal elliptic hole ω with semimajor and semiminor axes, respectively, a and $a/2$ (values of a to be explained shortly); a similar example was also used in [22]. A homogenous Neumann condition was prescribed on the internal elliptic hole, and outer boundary conditions were set as follows (also depicted in Fig. 3):

$$P_1P_2 : \partial u/\partial n = 0; \quad P_2P_3 : u = 0;$$
$$P_3P_4 : \partial u/\partial n = 1; \quad P_4P_1 : u = 0.$$

The quantity of interest was defined over a circular local region $S \subset \Omega_\omega$ as:

$$\mathcal{Q}(u) := |S|^{-1} \int_S u dS. \tag{32}$$

We first test performance of the proposed DEE at variations of the feature's sizes. In this test, the elliptic hole's center was fixed at $(0.5, 0)$, and the semi-major axis a was varied between 0.05 and 0.15 with a step size of 0.025 (denoted 0.05:0.025:0.15). The number of mesh elements and the degree of freedoms used to obtain the reference values for this example under COMSOL's defaulting settings are reported in Table 2. The computed errors e, the effectivity indices I in (29), and the estimated quantities $\mathcal{Q}(u) + e$ obtained by different approaches are summarized and compared in Fig. 4.

Fig. 4(a) or (c) shows that the estimated errors or quantities using the proposed estimator DEE were always very close to the reference value computed using direct FE analysis, for all values of a. We also see in Fig. 4(b) that the effectivity indices of all these approaches were always above 1. In particular the index for DEE lies within a small range from 1.0 to 1.2, demonstrating its high accuracy in defeaturing error estimate. FSA, TSA and Direct, however, behave differently—as the value of a increases, the estimated errors or quantities drastically moved away from the reference values; their corresponding effectivity indices range from 1.0 to 2.6. The proposed estimator DEE showed much better performance

Table 1
Average times taken to compute different estimates for the various examples tested in this section.

Numerical example	FEA	DEE	Direct	FSA	TSA
Poisson in Fig. 3	0.173	0.170	0.166	0.171	0.164
Elasticity in Fig. 7	0.281	0.187	0.140	0.208	0.140
Semilinear in Fig. 10	0.686	0.572	0.546		

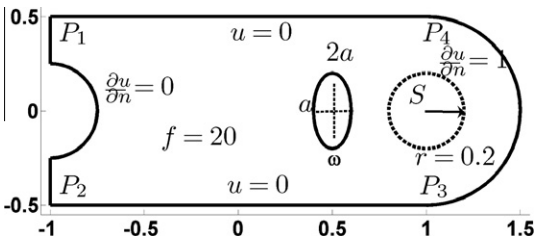

Fig. 3. An example to test performance of the proposed defeaturing error estimator for a Poisson equation.

Table 2
The number of mesh elements (NMEs) and degree of freedoms (DOFs) of the original geometry used to obtain the numerical results in Fig. 4; the NMEs and DOFs for the simplified geometry are, respectively, 642 and 1341.

Size a	.05	.06	.07	.08	.09	.1	.11	.12	.13	.14	.15
NMEs	1198	1162	1100	1058	1037	1002	982	944	906	921	878
DOFs	2482	2410	2286	2202	2161	2092	2052	1976	1900	1931	1846

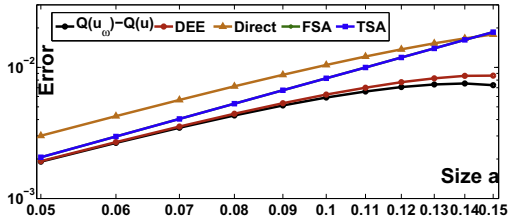

(a) Defeaturing errors e

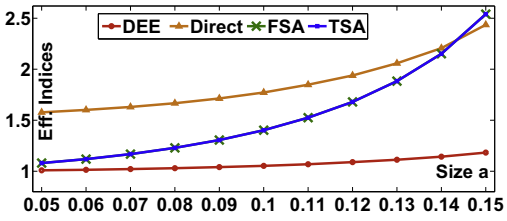

(b) Effectivity indices I defined in (29)

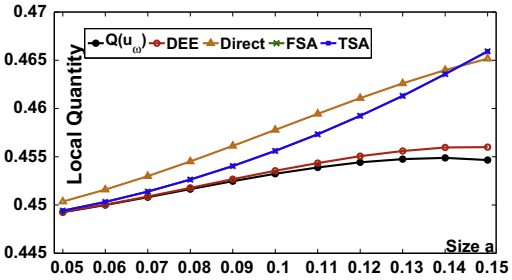

(c) Estimated quantities $\mathcal{Q}(u) + e$ for $\mathcal{Q}(\cdot)$ defined in (32)

Fig. 4. Numerical results for the Poisson equation in Fig. 3 for a local quantity $\mathcal{Q}(\cdot)$ defined in (32) for a varying internal elliptic hole of size (a = 0.05:0.025:0.15), for DEE computed via (22), Direct via (27), TSA via (30) and FSA via (31). The reference values computed by direct FEA are denoted $\mathcal{Q}(u_\omega) - \mathcal{Q}(u)$ in (a) and $\mathcal{Q}(u_\omega)$ in (c).

than Direct as it uses additional exterior approximations to dual errors.

The estimates obtained with TSA and FSA were always approximately in agreement over the whole range of a for this example. The former, however, was cheaper to compute as it does not involve solution of other auxiliary exterior problems; see also the summary of computational costs in Table 1 (outcomes reported in [22] only compared their approach to TSA based on circle approximation without directly considering the more accurate TSA for the elliptic hole cases).

We next test performance of the proposed DEE at variations of the feature's locations for this example. In this test, the elliptic hole's axis lengths were set to $(0.1, 0.2)$. We varied both the x- and y-coordinates of its center using x = −0.4:0.1:0.5 and y = 0:0.02:0.12. Taking the estimated error, effectivity index or local quantity as z-coordinate for each pair of parameters x, y, an error surface, effectivity surface and quantity surface were produced and compared in Fig. 5 for the different approaches. Similar results were observed to those in Fig. 4. Specifically, the effectivity indices for all approaches were always above 1, 1.0–1.1 for DEE, 1.1–2.7 for Direct, and 1.2–1.6 for both TSA and FSA, showing the greater accuracy of DEE.

DEE can also handle the case when non-homogeneous Neumann conditions are prescribed on the boundary of the negative feature ω. For the example in Fig. 3, the Neumann boundary term d was set to

$$g = 2^i(i-1)r \tag{33}$$

for a random number $0 < r < 1$ and for $i = 1, 2, \ldots, 11$. One of the set of applied loadings and the corresponding effectivity indices were shown in Figs. 6(a) and (b). Here, the results obtained by DEE and Direct approximated the reference value slightly better than TSA, but none of them provided effectivity indices strictly above 1 (FSA only works for free negative features and cannot be employed in this case). The similarity of the effectivity indices, particularly for loadings of large value, can perhaps be explained by the fact that the errors in this situation are mainly affected by the values of d on boundary $\partial\omega$ instead of the size of the feature.

5.2. Linear elasticity

We next show numerical results for a linear elasticity problem, comparing results obtained by DEE in (24) with those obtained by TSA [34], FSA [45] and Direct [30] (also given in (28)). The error estimates provided by TSA and FSA are listed below for reference.

TSA [34]. For an interior circular hole of radius r centered at point $\boldsymbol{P}_C$, TSA gives the following result for plane stress:

$$(\textbf{TSA} : \textbf{Elasticity}) \quad \mathcal{Q}(\boldsymbol{u}_\omega) - \mathcal{Q}(\boldsymbol{u}) = -\pi r^2 \left(\frac{4}{1+\nu} \sigma(\boldsymbol{u}) \cdot \epsilon(\boldsymbol{p}) + \frac{1-3\nu}{1-\nu^2} \mathbf{tr}(\sigma(\boldsymbol{u})) \mathbf{tr}(\epsilon(\boldsymbol{p})) \right) |_{\boldsymbol{P}_C}, \tag{34}$$

where $\epsilon(\boldsymbol{p})$ is the stress tensor, and $\mathbf{tr}(\cdot)$ is the trace operator.

FSA [45]. For an interior arbitrarily-shaped small hole free of external loadings, FSA gives:

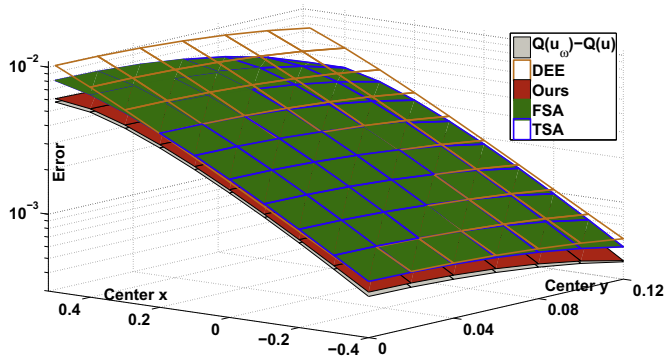

(a) Defeaturing errors

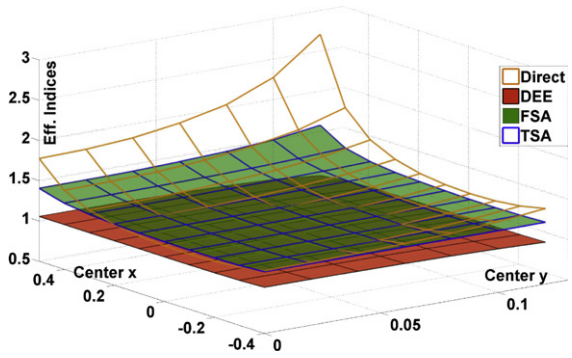

(b) Effectivity indices I defined in (29)

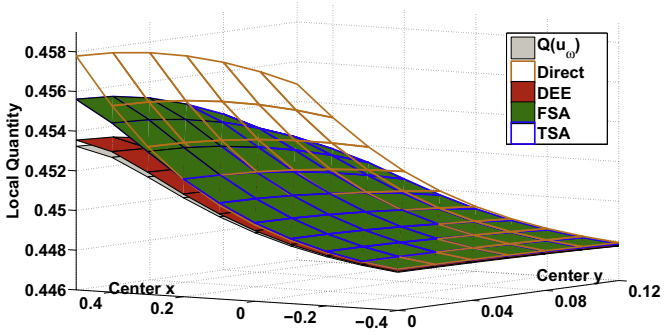

(c) Estimated quantities $\mathcal{Q}(u) + e$ for $\mathcal{Q}(\cdot)$ defined in (32)

Fig. 5. Numerical results for the Poisson equation in Fig. 3 for a local quantity $\mathcal{Q}(\cdot)$ defined in (32) for a varying elliptic hole at location (x = −0.4:0.1:0.5, y = 0:0.02:0.12) for DEE computed via (22), Direct via (27), TSA via (30) and FSA via (31). The reference values computed by direct FEA are denoted $\mathcal{Q}(u_\omega) - \mathcal{Q}(u)$ in (a) and $\mathcal{Q}(u_\omega)$ in (c).

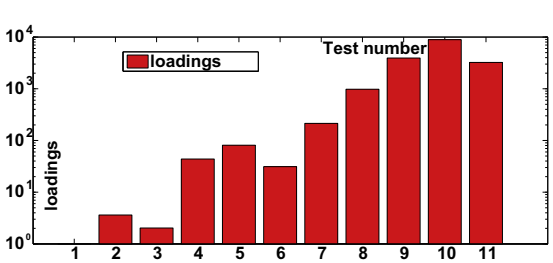

(a) External loadings d in (33)

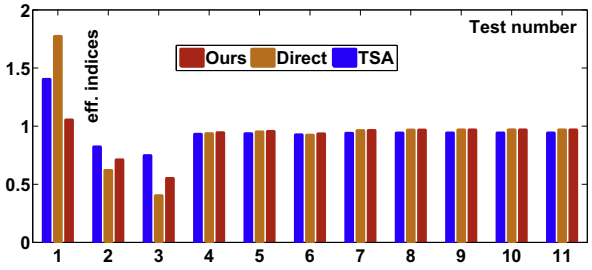

(b) Effectivity indices I defined in (29)

Fig. 6. Numerical results for a Poisson equation in Fig. 3 for a local quantity $\mathcal{Q}(\cdot)$ defined in (32) at variations of an elliptic hole's external loadings d in (33), for DEE computed via (22), Direct via (27) and TSA via (30).

$$(\textbf{FSA} : \textbf{Elasticity}) \quad \mathcal{Q}(\boldsymbol{u}_\omega) - \mathcal{Q}(\boldsymbol{u}) = \int_{\partial\omega} (\boldsymbol{V}\cdot\mathbf{n})(F_1 + F_2)\, ds \qquad (35)$$

where

$$F_1 := \frac{\boldsymbol{f}\cdot\boldsymbol{p} - (\sigma(\boldsymbol{u}) + \sigma(\boldsymbol{u}_E))\cdot(\Delta\boldsymbol{p} + \Delta\boldsymbol{p}_E)}{2},$$

$$F_2 := \frac{\boldsymbol{f}\cdot\boldsymbol{p}_E}{3},\ \boldsymbol{V} := \boldsymbol{P} - \boldsymbol{P}_C,$$

for a point $\boldsymbol{P}$ along the boundary $\partial\omega$, where $\boldsymbol{u}_E, \boldsymbol{p}_E$ are the corresponding primal and dual exterior solutions.

This example considered a plane stress problem, described in Fig. 7, of an internal elliptic hole ω with semimajor axis and semiminor axis, respectively, a and $a/2$, similar to the example used in [45]. When applying TSA, a spherical hole with the same cross-section was used as the negative feature instead of the ellip-

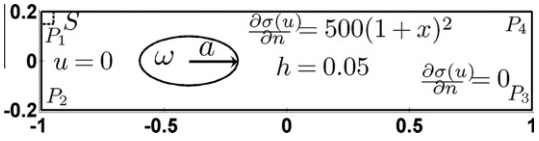

Fig. 7. An example to test performance of the proposed defeaturing error estimator for a linear elasticity problem.

Table 3
The number of mesh elements (NMEs) and degree of freedoms (DOFs) of the original geometry to obtain the numerical results in Fig. 8; the NMEs and DOFs of the simplified geometry are, respectively, 153 and 696.

Size a	.01	.015	.02	.025	.03	.035	.04	.045	.05
NMEs	1141	1031	961	974	899	865	827	805	758
DOFs	4722	4282	4002	4060	3758	3622	3470	3382	3236

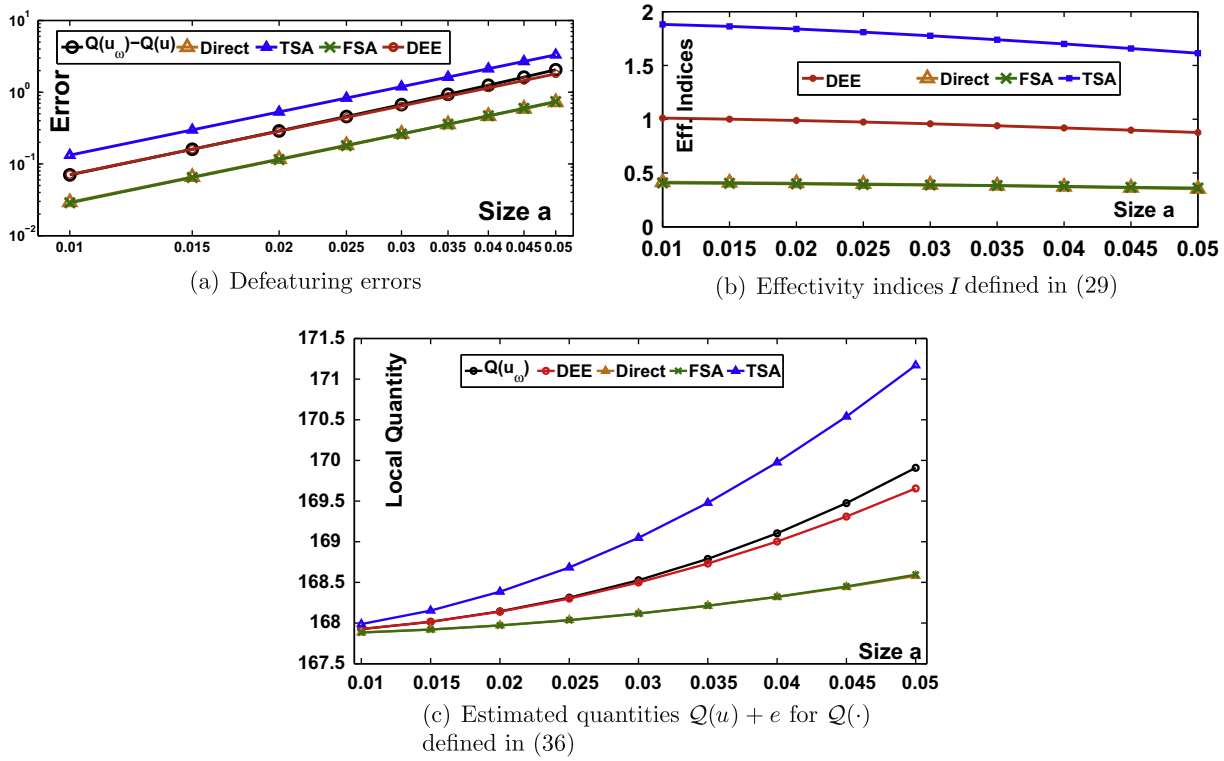

(a) Defeaturing errors

(b) Effectivity indices I defined in (29)

(c) Estimated quantities $\mathcal{Q}(u)+e$ for $\mathcal{Q}(\cdot)$ defined in (36)

Fig. 8. Numerical results for a linear elasticity problem in Fig. 7 for a local quantity $\mathcal{Q}(\cdot)$ defined in (36) for a varying internal elliptic hole of size (a = 0.01:0.005:0.05), for DEE computed via (24), Direct via (28), TSA via (34) and FSA via (35). The reference values computed by direct FEA are denoted $\mathcal{Q}(\boldsymbol{u}_\omega)-\mathcal{Q}(\boldsymbol{u})$ in (a) and $\mathcal{Q}(\boldsymbol{u}_\omega)$ in (c).

tic hole. The boundary for the internal elliptic hole was set free, and outer boundary conditions were set as follows:

$$P_1P_2:\boldsymbol{u}=\mathbf{0};\quad P_2P_3:\partial\sigma(\boldsymbol{u})/\partial\mathbf{n}=\mathbf{0};$$
$$P_3P_4:\partial\sigma(\boldsymbol{u})/\partial\mathbf{n}=\mathbf{0};\quad P_4P_1:\partial\sigma(\boldsymbol{u})/\partial\mathbf{n}=(0,-500(1+x)^2).$$

The quantity of interest was defined in the right-top square S of length 0.05 as follows

$$Q(\boldsymbol{u}):=|S|^{-1}\int_S\boldsymbol{\sigma}_{11}(\boldsymbol{u})\,d\Gamma. \tag{36}$$

We first test performance of the proposed DEE at variations of the feature's sizes. In this test, the elliptic hole was fixed at $(-0.6,0.05)$, and the semi-major axis a was varied as a = 0.01:0.005:0.05. The number of mesh elements and the degree of freedoms used to obtain the reference values for this example under COMSOL's defaulting settings are reported in Table 3. Figs. 8(a) and (c) show that the estimates provided by DEE were always very close to the reference values computed using direct FE analysis, for all values of a, with effectivity indices close to but slightly lower than 1. In contrast, TSA overestimated the errors with effectivity indices near 2, and FSA underestimated the errors with effectivity indices near 0.5. We also observed that, unlike the numerical results of the Poisson equation, variations of the hole's sizes do not significantly influence the effectivity of each approach—as the value of a increases, the effectivity indices for each approach remained similar. For this particular example, the estimates obtained by FSA and Direct are generally approximately the same over the whole range of a. The latter, however, is cheaper to compute as it does not involve solving additional auxiliary exterior problems: see Table 1.

We next test performance of the proposed DEE at variations of the feature's size and orientation. In this test, the elliptic hole's center was fixed at $(0.05,0)$, and we varied both the semiminor axis length and orientation of the negative feature, respectively, using a = 0.01:0.005:0.05 and $\theta = 0:\pi/12:\pi/2$. Taking the estimated error, effectivity index and estimated local quantity as z-coordinate for each pair of x and θ, a set of error surfaces, effectivity surfaces, and quantity surfaces were produced and compared in Fig. 9. It can be seen that none of the approaches strictly bounded the reference value —TSA generally produced relatively larger error estimates than other approaches but also underestimated the errors for $\theta=\pi/6$. The effectivity indices of DEE and Direct generally performed more robustly than TSA and FSA—the associated effectivity indices of the former two were near 1 and 0.5 throughout while those of the latter two varied much more. Additionally, DEE showed much closer approximation to the reference value than all the other approaches, with associated effectivity indices always near the ideal value of 1.

5.3. A semilinear second order elliptic equation

This final example tests performance of DEE for a nonlinear case, as defined in (2) with $\lambda=1$; the uniqueness and stability of the solution can be easily ensured in this case [11]. An analytical

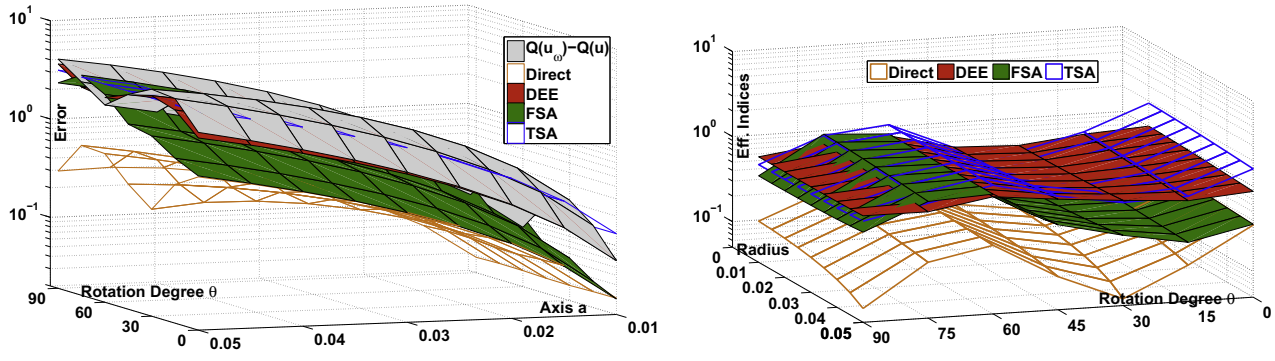

(a) Defeaturing errors

(b) Effectivity indices I defined in (29)

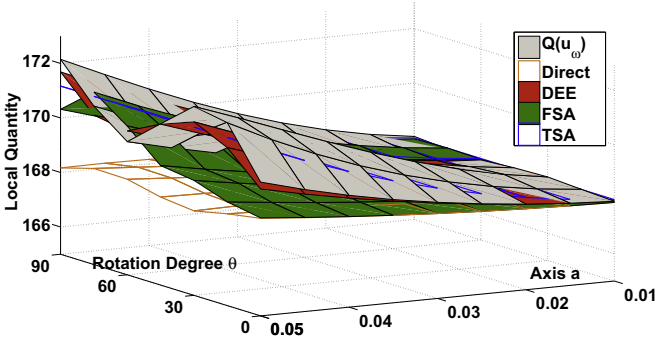

(c) Estimated quantities $\mathcal{Q}(u)+e$ for $\mathcal{Q}(\cdot)$ defined in (36)

Fig. 9. Numerical results for a linear elasticity problem in Fig. 7 for a local quantity $\mathcal{Q}(\cdot)$ defined in (36) for a varying internal elliptic hole of semiminor axis (a = 0.01:0.005:0.05) and rotation angle ($\theta = 0 : \pi/12 : \pi/2$), for DEE computed via (24), Direct via (28), TSA via (34) and FSA via (35). The reference values computed by direct FEA are denoted $\mathcal{Q}(\boldsymbol{u}_\omega) - \mathcal{Q}(\boldsymbol{u})$ in (a) and $\mathcal{Q}(\boldsymbol{u}_\omega)$ in (c).

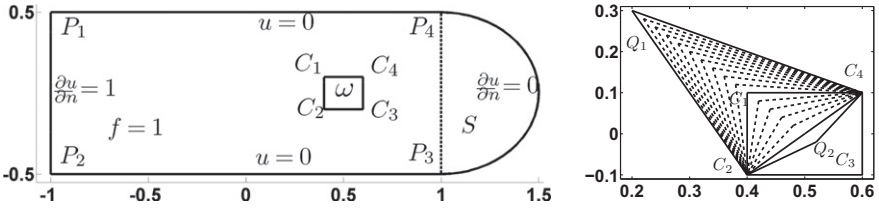

(a) Problem description

(b) Shape variation of a negative feature

Fig. 10. An example to test performance of the proposed defeaturing error estimator for the problem in Eq. (1) with $\lambda = 1$; (a) shows the test example, and (b) shows variation of the negative feature shape in our numerical examples.

TSA or FSA solution is not available for this nonlinear case, so we only compared our results with those obtained by Direct in the form of (26). In this example, the constant C_N involved in (26) was set to

$$C_N := \frac{\|p\|_{L^2(\partial\omega)}}{\|p\|_E}, \tag{37}$$

where $\|p\|_E$ denotes the energy norm of p.

The example, shown in Fig. 10, has a square negative feature ω of length a. A homogeneous Neumann boundary condition was prescribed on the boundary for the internal square hole, and the outer boundary conditions were set as follows (also depicted in Fig. 10):

$$P_1P_2 : \partial u/\partial n = 1; \quad P_2P_3 : u = 0;$$
$$P_3P_4 : \partial u/\partial n = 0; \quad P_4P_1 : u = 0.$$

A nonlinear functional $\mathcal{Q}(u)$ describing the quantity of interest in a half circular region S is given by

$$\mathcal{Q}(u) := |S|^{-1} \int_S u^2 \, d\Gamma. \tag{38}$$

The nonlinear example was first tested at variations of the square's size a; results are summarized in Fig. 11. Both DEE and Direct overestimated the defeaturing error, with corresponding effectivity indices, respectively, ranging from 1.2 to 2.2, and from 1.3 to 3.5. DEE achieved better performance than Direct by further use of the dual error estimate as described in (26).

The example was also tested at variations of the negative feature's shape. We moved the top-left corner point C_1 of the square along a straight line Q_1Q_2 with $Q_1 = (0.2, 0.3)$ and $Q_2 = (0.52, -0.02)$, as also illustrated in Fig. 10(b), and computed the defeaturing error for each location of C_1. The number of mesh

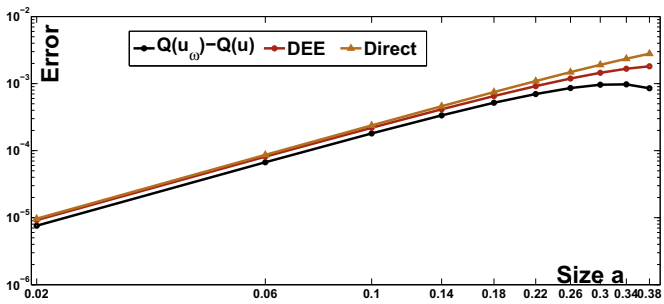

(a) Defeaturing errors

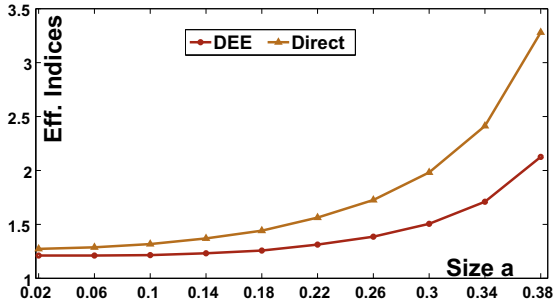

(b) Effectivity indices I in (29)

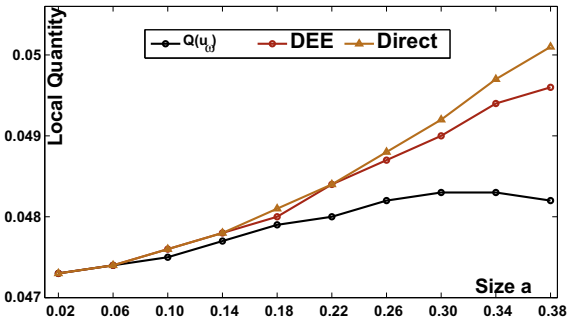

(c) Estimated quantities $\mathcal{Q}(u)+e$ for $\mathcal{Q}(\cdot)$ defined in (38)

Fig. 11. Numerical results for a nonlinear problem in Fig. 10 for a local quantity $\mathcal{Q}(\cdot)$ defined in (38) for a varying negative feature of size ($a = 0.02{:}0.04{:}0.38$), for DEE computed via (26) and Direct via (27). The reference values computed by direct FEA are denoted $\mathcal{Q}(u_\omega) - \mathcal{Q}(u)$ in (a) and $\mathcal{Q}(u_\omega)$ in (c).

Table 4
The number of mesh element (NMEs) and degree of freedoms (DOFs) of the original geometry to obtain the numerical results in Fig. 12, where X, Y, respectively, denotes the x, y-coordinate of the moving vertex C_1; the NMEs and DOFs of the simplified geometry are, respectively, 246 and 535.

X	.2	.24	.28	.32	.36	.4	.44	.48	.52
Y	0.3	.26	.22	.18	.14	.10	.06	.02	-.02
NMEs	267	278	273	279	278	294	286	300	304
DOFs	587	608	597	609	606	638	622	650	658

elements and the degree of freedoms used to obtain the reference values for this example under COMSOL's defaulting settings are reported in Table 4. The numerical results were summarized and compared in Fig. 12. Again, the associated effectivity indices of either DEE or Direct were always larger than 1. DEE achieved better results than Direct, with effectivity indices in the range of $(1.0, 2.2)$ to $(1.1, 2.6)$.

6. Conclusions and future work

A general framework was given for a posteriori estimate of goal-oriented defeaturing error caused by removal of a negative feature from a complex geometry. Experiments show that the proposed estimate generally approximates the reference value better, with effectivity index values closer to 1 than for other leading methods. The method is applicable to both linear and non-linear problems, although it works better in the former case. This improved performance is mainly due to two facts. First, the solutions u, p in the residual term of (22) are computed without approximation (ignoring numerical finite element approximation errors), whereas TSA and FSA focus on asymptotic behavior as feature size approaches zero and use first order approximation for both u and p. Second, the dual error e_D is further estimated based on Proposition 2 in linear cases or Proposition 3 in nonlinear cases. Additionally, the proposed estimators also demonstrated its effectivity at variations of the feature's sizes, locations, or shapes in spite of the assumptions in Proposition 2.

In certain cases, the effectivity index of the proposed estimator was lower than 1, and hence it underestimated the defeaturing errors. This observations can be mainly explained by three facts. First, in nonlinear cases, the higher order terms $\Delta\mathcal{R}_P/2$ and $r(\bar{e}_P, \bar{e}_D)$ in Proposition 1 were directly discarded without further estimate. Second, the dual error e_D involved in (18) was approximated using the exterior solution e_E in linear cases instead of being strictly bounded. Thirdly, the constants C_N involved in (26) were computed practically via (37). However, other alternative approaches do not always strictly bound the defeaturing error either. Building tight, strict, upper error bounds deserves further research effort, as they are critical in certain applications.

The proposed estimator only works for negative features with Neumann boundary conditions, where the original geometry is contained within the simplified geometry. Further work is needed for cases involving removal of protrusion features, features on the boundary, and multiple features. Exploring the use of the proposed estimator to guide design optimization is also of interest.

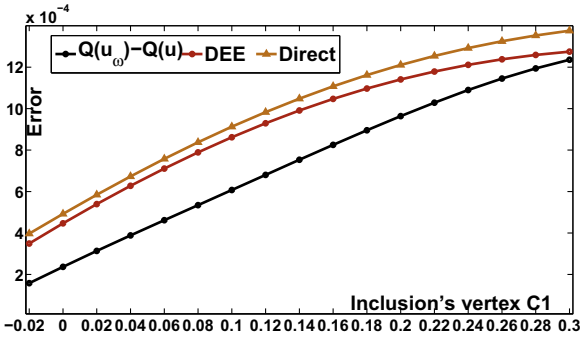

(a) Defeaturing errors

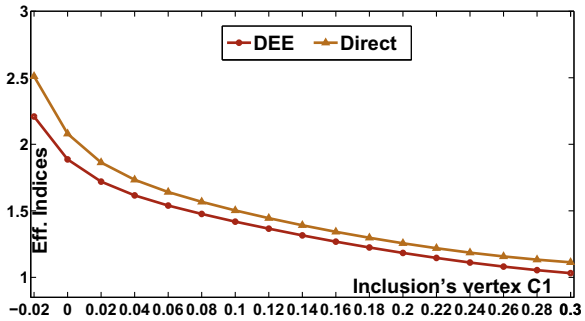

(b) Effectivity indices I in (29)

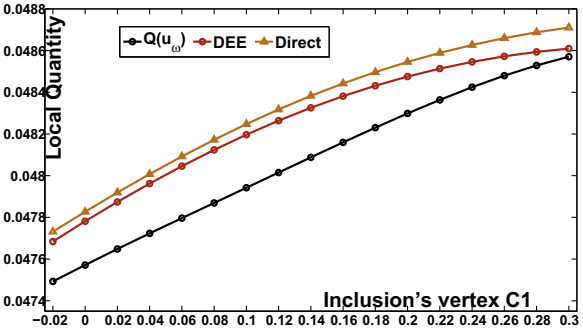

(c) Estimated quantities $\mathcal{Q}(u) + e$ for $\mathcal{Q}(\cdot)$ defined in (38)

Fig. 12. Numerical results for a nonlinear problem in Fig. 10 for a local quantity $\mathcal{Q}(\cdot)$ defined in (38) for a varying negative feature (with vertex C_1 moving from Q_1 to Q_2 in Fig. 10(b)), for DEE computed via (26) and Direct via (27). The reference values computed by direct FEA are denoted $\mathcal{Q}(u_\omega) - \mathcal{Q}(u)$ in (a) and $\mathcal{Q}(u_\omega)$ in (c).

Acknowledgements

The authors thank the referees for their comments and suggestions which helped improve the manuscript. The work was supported by the National Basic Research Program of China (2011CB302400) and the NSF of China (60736019, 11271157). We also wish to thank the high performance computing center of Jilin University, Prof. Xiao-shan Gao, Frank C. Langbein, Ralph R. Martin and Junzhe Zheng for their assistance.

Appendix A. Proof for Lemma 2

We first introduce the idea of the absorbing PML layer following [12]. We surround the domain $\Omega \subset B_{\rho_1}(O)$ with a PML layer $\Omega_P = \{x \in \mathbb{R}^2 \setminus \omega : \rho_1 < |x| < \rho_2\} = B_{\rho_2}(O) \setminus \overline{B_{\rho_1}(O)}$. The specially designed model medium in the PML layer should basically be chosen such that either the wave never reaches its external boundary or the amplitude of the reflected wave is so small that it does not essentially contaminate the solution in Ω_{ρ_1}. Throughout this paper, we assume $\rho_2 \leqslant C\rho_1$ for some generic fixed constant $C > 0$.

Let $\alpha(\rho) = 1 + i\sigma(\rho)$ be the fictitious medium property which satisfies

$$\sigma \in C(\mathbb{R}), \quad \sigma \geqslant 0, \quad \text{and} \quad \sigma = 0 \quad \textit{for} \quad \rho \leqslant \rho_1.$$

In order to use the PML formulation, we first introduce the complex radius transformation $\widetilde{\rho}$ defined by

$$\widetilde{\rho} := \begin{cases} \rho, & \text{if } \rho \leqslant \rho_1, \\ \int_0^\rho \alpha(s)ds = \rho\left[1 + \frac{i\sigma_0(\rho-\rho_1)^{m+1}}{(m+1)\rho(\rho_2-\rho_1)^m}\right] := \rho\beta(\rho), & \text{if } \rho_1 \leqslant \rho \leqslant \rho_2, \end{cases} \tag{A.1}$$

where we always adopt $\sigma_0 \approx 10^3$ and $m = 3, 4$ or 5 for practical purposes.

Using the relation

$$\frac{\widetilde{\rho}}{\rho} = \beta(\rho) \quad \text{and} \quad \frac{\partial\widetilde{\rho}}{\partial\rho} = \alpha(\rho),$$

we can rewrite (20) in the bounded domain for a polar coordinate system

$$\begin{cases} \widetilde{\mathcal{L}}e_{pml} = \bar{\mathcal{Q}} & \text{in } B_{\rho_2}(O) \setminus \omega, \\ \mathcal{B}e_{pml} = -\mathcal{B}p & \text{on } \partial\omega, \\ e_{pml} = 0 & \text{on } \partial B_{\rho_2}(O), \end{cases} \tag{A.2}$$

where e_{pml} denotes the PML solution on $B_{\rho_2}(O) \setminus \omega$ and $\widetilde{\mathcal{L}}$ is the counterpart of $\mathcal{L}$ under the change in (A.1). In order to give convergence results for the PML problem, we first make the following assumption:(H1) In practical applications, the fictitious medium property σ is usually taken as power function:

$$\sigma(\rho) = \sigma_0\left(\frac{\rho-\rho_1}{\rho_2-\rho_1}\right)^m, \rho_1 \leqslant \rho \leqslant \rho_2$$

, for$\sigma_0 > 0$ and integer $m \geqslant 1$,

which is an empirical formula used in the practical application of PML techniques.

Since $\mathcal{L}$ is linear with respect to e_D, using spherical harmonic analysis in a similar way to [12], we obtain the following conclusion:

Lemma 4. *Let e_E and e_{pml} be the solutions of (20) and (A.2) respectively, and assume (H1) is satisfied. Then for sufficiently large $\sigma_0 > 0$,*

$$\|e_E - e_{pml}\|_{H^1(B_{\rho_1}(O)\setminus\omega)} \leqslant C_1 \exp\left(-\frac{C_2\sigma_0\delta}{m+1}\left(1-\frac{(m+1)\rho_1^2}{\sqrt{(m+1)^2\rho_2^2+\sigma_0^2\delta^2}}\right)^{1/2}\right), \tag{A.3}$$

where C_1, C_2 are positive constants, and $\delta := \rho_2 - \rho_1$.

Basically, the convergent estimate of (A.3) depends on σ_0 and the width of the PML region $\delta := \rho_2 - \rho_1$. We always choose δ to be small and $\delta\sigma_0$ large enough to guarantee the accuracy between e_E and e_{pml}. The PML solution e_{pml} decays to zero exponentially in the PML domain Ω_P. Furthermore, the operator of $\tilde{\mathcal{L}}_1$ is exactly the operator $\mathcal{L}_1$ in $B_{\rho_1}(O)\setminus\omega$, because the complex transformation in the ρ direction operates only in the PML region Ω_P.

Lemma 5. *Let $G_D(x,y;\xi,\eta)$ and $G_{pml}(x,y;\xi,\eta)$ denote Green's functions for (19) and (A.2), respectively, and $\bar{G}(\cdot,\cdot) = G_D(x-\cdot, y-\cdot) - G_{pml}(x-\cdot, y-\cdot)$. Then*

$$|e_D(x,y) - e_{pml}(x,y)| \leqslant \|\bar{G}\|_{L^2(\Omega_\omega)}\|\bar{\mathcal{Q}}\|_{L^2(\Omega_\omega)} + \|\bar{G}\|_{L^2(\partial\omega)}\|\mathcal{B}p\|_{L^2(\partial\omega)}. \tag{A.4}$$

Proof. Using Green's formulations for (19) and (A.2), for (x,y) on $\partial\omega$, we have

$$e_D(x,y) = \int_{\Omega_\omega} G_D(x-\xi, y-\eta)\bar{\mathcal{Q}}(\xi,\eta)d\xi d\eta - \int_{\partial\omega} G_D(x-\xi, y-\eta)(\mathcal{B}e_D(\xi,\eta))ds,$$

$$e_{pml}(x,y) = \int_{B_\rho(O)\setminus\omega} G_{pml}(x-\xi, y-\eta)\bar{\mathcal{Q}}(\xi,\eta)d\xi d\eta - \int_{\partial\omega} G_{pml}(x-\xi, y-\eta)(\mathcal{B}e_{pml}(\xi,\eta))ds.$$

Noting that f vanishes on $B_{\rho_2}(O)\setminus\Omega$, and subtracting the above two equations, we get

$$|e_D(x,y) - e_{pml}(x,y)| \leqslant \left|\int_{\Omega_\omega} \bar{G}(\xi,\eta)\bar{\mathcal{Q}}(\xi,\eta)d\xi d\eta\right| + \left|\int_{\partial\omega} \bar{G}(\xi,\eta)\mathcal{B}p(\xi,\eta)ds\right|.$$

Using the Cauchy inequality implies the conclusion. □

Further using the triangle inequality and trace theorem in Lemmas 4 and 5, we can easily obtain the result in Lemma 2.

Appendix B. Proof for Proposition 3

From Lemma 3 and discarding the higher order term $\Delta\mathcal{R}_D$ in (25), the dual error $e_D := p_\omega - p$ is governed by the following linear equation,

$$\alpha'_\omega(u; v, e_D) = \mathcal{R}_D(u,p;v), \quad v \in H^1_E(\Omega_\omega). \tag{B.1}$$

Following the proof of Lemma 1, we have

$$\mathcal{R}_D(u,p;v) = \int_{\partial\omega}(g-\bar{g})v\, d\Gamma, \quad v \in H^1_E(\Omega_\omega)$$

with $g = \mathcal{B}p_\omega|_{\partial\omega}$ and $\bar{g} = \mathcal{B}p|_{\partial\omega}$ the given Neumann boundary conditions for p_ω and p, respectively. By the trace theorem (see [17]) and the equivalence of the H^1 norm and the energy norm (denoted by $\|\cdot\|_E$), there exists a constant C_N such that

$$\|v\|_{L^2(\partial\omega)} \leqslant C_N\|v\|_E, \quad v \in H^1_E(\Omega_\omega). \tag{B.2}$$

Thus, we have

$$|\alpha'_\omega(u; v, e_D)| = \left|\int_{\partial\omega}(g-\bar{g})v\, d\Gamma\right| \leqslant \|g-\bar{g}\|_{L^2(\partial\omega)}\|v\|_{L^2(\partial\omega)} \leqslant C_N\|g-\bar{g}\|_{L^2(\partial\omega)}\|v\|_E.$$

Replacing v by e_D in the above equation gives

$$\|e_D\|_E^2 = \alpha'_\omega(u; e_D, e_D) \leqslant C_N\|g-\bar{g}\|_{L^2(\partial\omega)}\|e_D\|_E,$$

or equivalently,

$$\|e_D\|_E \leqslant C_N\|g-\bar{g}\|_{L^2(\partial\omega)}.$$

Thus,

$$\left|\int_{\partial\omega}(d-d_0)e_D\, d\Gamma\right| \leqslant \|d-d_0\|_{L^2(\partial\omega)}\|e_D\|_{L^2(\partial\omega)} \leqslant \|d-d_0\|_{L^2(\partial\omega)}C_N\|e_D\|_E \leqslant C_N^2\|d-d_0\|_{L^2(\partial\omega)}\|g-\bar{g}\|_{L^2(\partial\omega)}.$$

Further taking into account (18) verifies Proposition 3.

References

[1] COMSOL Multiphysics 3.5a, 2007. Available at: <http://www.comsol.com>.
[2] M. Ainsworth, M. Arnold, Computable error bounds for some simple dimensionally reduced models on thin domains, IMA Journal of Numerical Analysis 21 (1) (2001) 81–105.
[3] S. Amstutz, Sensitivity analysis with respect to a local perturbation of the material property, Asymptotic Analysis 49 (1-2) (2006) 87–108.
[4] M. Badiale, E. Serra, Semilinear Elliptic Equations for Beginners, Springer, 2011.
[5] Y. Bazilevs, V. Calo, J. Cottrell, J. Evans, T. Hughes, S. Lipton, M. Scott, T. Sederberg, Isogeometric analysis using T-splines, Computer Methods in Applied Mechanics and Engineering 199 (5-8) (2010) 229–263.
[6] A. Becker, The Boundary Element Method, McGraw Hill, New York, 1992.
[7] R. Becker, R. Rannacher, An optimal control approach to a posteriori error estimation in finite element methods, Acta Numerica 10 (2001) 1–102.
[8] J. Berenger, A perfectly matched layer for the absorption of electromagnetic waves, Journal of Computational Physics 114 (2) (1994) 185–200.
[9] P. Bettess, Infinite Elements, Penshaw Press, Sunderfand, UK, 1992.
[10] M. Braack, A. Ern, A posteriori control of modeling errors and discretization errors, Multiscale Modeling & Simulation 1 (2) (2003) 221–238.
[11] G. Caloz, J. Rappaz, Numerical analysis for nonlinear and bifurcation problems, in: Handbook of Numerical Analysis, 1997, pp. 487–638.
[12] Y. Cao, R. Zhang, K. Zhang, Finite element method and discontinuous Galerkin method for Stochastic scattering problem of Helmholtz type in R^d, Potential Analysis 28 (4) (2008) 301–319.
[13] J.A. Cottrell, T.J.R. Hughes, A. Reali, Studies of refinement and continuity in isogeometric analysis, Computer Methods in Applied Mechanics and Engineering 196 (41–44) (2007) 4160–4183.
[14] W.E.B. Engquist, Multiscale modeling and computation, Notices of the AMS 50 (9) (2003) 1062–1070.
[15] W.E.B. Engquist, X. Li, W. Ren, E. Vanden-Eijnden, Heterogeneous multiscale methods: a review, Computer Physics Communications 2 (3) (2007) 367–450.
[16] H. Eschenauer, N. Olhoff, Topology optimization of continuum structures: a review, Applied Mechanics Review 54 (4) (2001) 331–390.
[17] L. Evans, Partial Differential Equations, American Mathematical Society, New York, 1998.
[18] J. Faria, A. Novotny, R. Feijoo, E. Taroco, C. Padra, Second order topological sensitivity analysis, International Journal of Solids and Structures 44 (14–15) (2007) 4958–4977.
[19] R. Feij, A. Novotny, E. Taroco, C. Padra, The topological derivative for the Poisson's problem, Mathematical Models and Methods in Applied Sciences 13 (12) (2003) 1825–1844.
[20] R. Ferrandes, P. Marin, J. Leon, F. Giannini, A posteriori evaluation of simplification details for finite element model preparation, Computers & Structures 87 (1–2) (2009) 73–80.
[21] M. Giles, E. Suli, Adjoint methods for PDEs: a posteriori error analysis and postprocessing by duality, Acta Numerica 11 (2002) 145–236.
[22] S. Gopalakrishnan, K. Suresh, Feature sensitivity: a generalization of topological sensitivity, Finite Elements in Analysis and Design 44 (11) (2008) 696–704.
[23] T. Hou, X. Wu, A multiscale finite element method for elliptic problems in composite materials and porous media, Journal of Computational Physics 189 (1) (1997) 169–189.
[24] T. Hughes, J. Cottrell, Y. Bazilevs, Isogeometric analysis: CAD, finite elements, NURBS, exact geometry and mesh refinement, Computer Methods in Applied Mechanics and Engineering 194 (39–41) (2005) 4135–4195.
[25] J. Keller, Removing small features from computational domains, Journal of Computational Physics 113 (1) (1994) 148–150.

[26] D. Kelly, J. De, S. Gago, O. Zienkiewicz, I. Babuska, A posteriori error analysis and adaptive processes in the finite element method: Part I: error analysis, International Journal for Numerical Methods in Engineering 19 (11) (1983) 1593–1619.
[27] H. Kim, Y. Seo, S. Youn, Isogeometric analysis with trimming technique for problems of arbitrary complex topology, Computer Methods in Applied Mechanics and Engineering 199 (45–48) (2010) 2796–2812.
[28] S. Lee, A CAD–CAE integration approach using feature-based multi-resolution and multi-abstraction modelling techniques, Computer-Aided Design 37 (9) (2005) 941–955.
[29] M. Li, S. Gao, Estimating defeaturing-induced engineering analysis error for arbitrary 3D features, Computer-Aided Design 43 (12) (2011) 1587–1597.
[30] M. Li, S. Gao, R. Martin, Estimating effects of removing negative features on engineering analysis, Computer-Aided Design 43 (1) (2011) 1402–1412.
[31] X. Li, J. Zheng, T. Sederberg, T. Hughes, M. Scott, On linear independence of T-spline blending functions, Computer Aided Geometric Design 29 (1) (2012) 63–76.
[32] R. McCune, C. Armstrong, D. Robinson, Mixed-dimensional coupling in finite element models, International Journal for Numerical Methods in Engineering 49 (6) (2000) 725–750.
[33] S. Nazarov, Asymptotic analysis of shape functionals, Journal de Mathématiques Pures et Appliqués 82 (2) (2003) 125–196.
[34] A. Novotny, R. Feijoo, E. Taroco, C. Padra, Topological sensitivity analysis for three-dimensional linear elasticity problem, Computer Methods in Applied Mechanics and Engineering 196 (41–44) (2007) 4354–4364.
[35] J. Oden, S. Prudhomme, Estimation of modeling error in computational mechanics, Journal of Computational Physics 182 (2) (2002) 496–515.
[36] J. Oden, S. Prudhomme, A. Romkes, P. Bauman, Multiscale modeling of physical phenomena: adaptive control of models, SIAM Journal on Scientific Computation 28 (6) (2005) 2359–2389.
[37] S. Prudhomme, J. Oden, T. Westermann, J. Bass, M. Botkin, Practical methods for a posteriori error estimation in engineering applications, International Journal for Numerical Methods in Engineering 56 (8) (2003) 1193–1224.
[38] X. Qian, Full analytical sensitivities in NURBS based isogeometric shape optimization, Computer Methods in Applied Mechanics and Engineering 199 (29–32) (2010) 2059–2071.
[39] W. Quadros, S. Owen, Defeaturing CAD models using a geometry-based size field and facet-based reduction operators, in: Proceedings of the 18th International Meshing Roundtable, 2009, pp. 301–328.
[40] T. Sederberg, J. Zheng, A. Bakenov, A. Nasri, T-splines and T-NURCCSs, ACM Transaction on Graphics 22 (3) (2003) 477–484.
[41] V. Shapiro, I. Tsukanov, A. Grishin, Geometric issues in computer aided design/computer aided engineering integration, Journal of Computing and Information Science in Engineering 11 (2) (2011) 1–13. 021005.
[42] J. Sokolowski, A. Zochowski, On topological derivative in shape optimization, SIAM Journal of Control Optimization 37 (4) (1999) 1251–1272.
[43] I. Temizer, P. Wriggers, T. Hughes, Contact treatment in isogeometric analysis with NURBS, Computer Methods in Applied Mechanics and Engineering 200 (9–12) (2011) 1100–1112.
[44] A. Thakur, A. Banerjee, S. Gupta, A survey of CAD model simplification techniques for physics-based simulation applications, Computer-Aided Design 41 (2) (2009) 65–80.
[45] I. Turevsky, S. Gopalakrishnan, K. Suresh, Defeaturing: a posteriori error analysis via feature sensitivity, International Journal for Numerical Methods in Engineering 76 (9) (2008) 1379–1401.
[46] I. Turevsky, S. Gopalakrishnan, K. Suresh, An efficient numerical method for computing the topological sensitivity of arbitrary-shaped features in plate bending, International Journal for Numerical Methods in Engineering 79 (13) (2009) 1683–1702.
[47] K. Vemaganti, Modelling error estimation and adaptive modelling of perforated materials, International Journal for Numerical Methods in Engineering 59 (12) (2004) 1587–1604.
[48] W. Wang, Y. Zhang, L. Liu, T. Hughes, Trivariate solid T-spline construction from boundary triangulations with arbitrary genus topology, Computer-Aided Design: Special Issue of Solid and Physical Modeling 45 (2) (2013) 351–360.
[49] Gang Xu, Bernard Mourrain, Rgis Duvigneau, Andr Galligo, Analysis-suitable volume parameterization of multi-block computational domain in isogeometric applications, Computer-Aided Design: Special Issue of Solid and Physical Modeling 45 (2) (2013) 395–404.
[50] Y. Zhang, W. Wang, T. Hughes, Conformal solid T-spline construction from boundary T-spline representations, Computational Mechanics (2012), http://dx.doi.org/10.1007/s00466-012-0787-6.
[51] Y. Zhang, W. Wang, T. Hughes, Solid T-spline construction from boundary representations for genus-zero geometry, Computer Methods in Applied Mechanics and Engineering (2012), http://dx.doi.org/10.1016/j.cma.2012.01.014, 2012.